

Quantitative Kelvin Probe Force Microscopy of back-gated 2D semiconductors

Zander Scholl^{1a}, Ezra Frohlich^{1a}, Natalie Rogers^{1a}, Paul Nguyen², Baker Hase², Joseph Tatsuro Murphy³, Joel Toledo-Urena³, David Cobden², Jennifer T. Heath^{1*}

¹Department of Physics, Reed College, Portland, OR 97202 USA

²Department of Physics, University of Washington, Seattle, Washington 98195, USA

³Department of Physics, Linfield University, McMinnville, OR 97128, USA

*Correspondence to: jheath@reed.edu

In 2D field effect transistors the gate electrostatically dopes the 2D semiconductor (2DSC) channel, tuning the Fermi level. In principle, Kelvin probe force microscopy (KPFM) can detect the Fermi level, and its dependence on gate bias as well as position, potentially directly yielding band gaps, contact barriers, spatial nonuniformities, and sub-gap densities of states in such devices. However, KPFM relies on an oscillating probe voltage which itself electrostatically dopes the 2DSC, potentially creating a nonlinear response. Here, we show that when a suitably thin hBN back-gate dielectric is used, the KPFM signal agrees well with expectations, as explained by a quasistatic charge-balance model. Corresponding experimental results show excellent consistency with the literature values of the bandgaps of monolayer and trilayer WSe₂. With this approach, the widely available technique of KPFM should find improved utility and new uses in the study of 2D devices.

Interest in 2D materials systems has exploded in recent years, as researchers have explored new layered materials and stacked them together in various combinations. Investigations range from manufacturable, room-temperature devices to systems exhibiting exotic physical behavior at low temperatures [1,2,3]. A tool that would seem to be convenient and well suited for studying 2D materials and devices is Kelvin probe force microscopy (KPFM) [4], which in principle can map the electric potential variation with position or applied voltages.

In KPFM an AC voltage is applied between the metallic probe tip and the sample, creating an oscillating tip-sample force and force gradient which is detected via the tip's vibration amplitude (AM-KPFM) or resonance frequency shift (FM-KPFM). KPFM works well for metallic or semi-metallic surfaces, including graphene [5,6,7]. However, doped semiconductors can have an asymmetric, nonlinear response to the tip voltage due to the metal-insulator-semiconductor (MIS)-like tip-surface interaction, requiring caution in interpreting the KPFM signal, V_{KP} , as a direct quantitative measure of the Fermi level

^a Z.S., E.F., and N.R. contributed equally to this work.

[8]. While 2D semiconductors (2DSCs) have similarities to their bulk counterparts, they differ in that, by simple geometry, they cannot support surface depletion regions that screen external fields.

In current-voltage measurements of 2D FETs, contributions from contacts and spatial non-uniformity are hard to separate from the intrinsic response of the 2DSC channel.

Meanwhile, tunneling current measurements can provide spatial maps but are still hampered by nonideal contacts [9]. In this light, KPFM has been employed on multiple occasions to attempt to deconvolute the various factors influencing device current-voltage performance, for example by imaging relative band alignments and contact barriers [10,11], characterizing depletion regions at interfaces [12], and measuring relative changes in work functions with chemical doping [13].

KPFM can also be fruitfully applied to measure the change in work function, and thus Fermi level E_F , while varying the bias on a gate, V_g , in a simple back-gate transistor geometry (Fig. 1a). In this way it has been used to investigate sub-bandgap defect densities [14] and to explore charge trapping [15] in MoS₂ flakes exfoliated on SiO₂.

Despite these apparent successes, there is reason to question the reliability of KPFM data on 2DSCs. Given that the AC component of tip bias, \tilde{V}_{tip} , is typically large enough to cause significant local band bending in the 2DSC, as shown schematically in Fig. 1b, the interplay of gate and tip voltages could distort the KPFM measurement. An important initial check is to observe V_{KP} when E_F is deep within the bandgap of the 2DSC. In this case there is no screening by free charge and V_{KP} should directly track V_g . In the literature, V_{KP} appeared to vary linearly over a range of V_g , but the slope dV_{KP}/dV_g was smaller than the expected value of unity (at ~ 0.2 for monolayer MoS₂ in both [14] Fig. S2, and [15] Fig. 4b), suggesting possible ambiguity in the interpretation of KPFM data.

For further useful deployment of KPFM in 2D materials systems, there is an urgent need to eliminate this ambiguity. Here, therefore, we take a step back and set out to carefully establish the conditions under which KPFM can reliably determine E_F as V_g is varied.

In KPFM, the tip is biased with a sum of DC and AC components,

$$V_{\text{tip}} = V_{\text{DC}} + \tilde{V}_{\text{tip}} \sin(\omega_e t). \quad (1)$$

This modulates the Coulomb interaction between the tip and sample, driving a mechanical tip oscillation at frequency ω_e . The value of V_{DC} is continuously adjusted in a feedback loop to minimize the resulting tip oscillations; ideally the minimum occurs when the charge on the tip is zero [4]. V_{KP} is defined as this optimized value of V_{DC} . For a metallic sample the

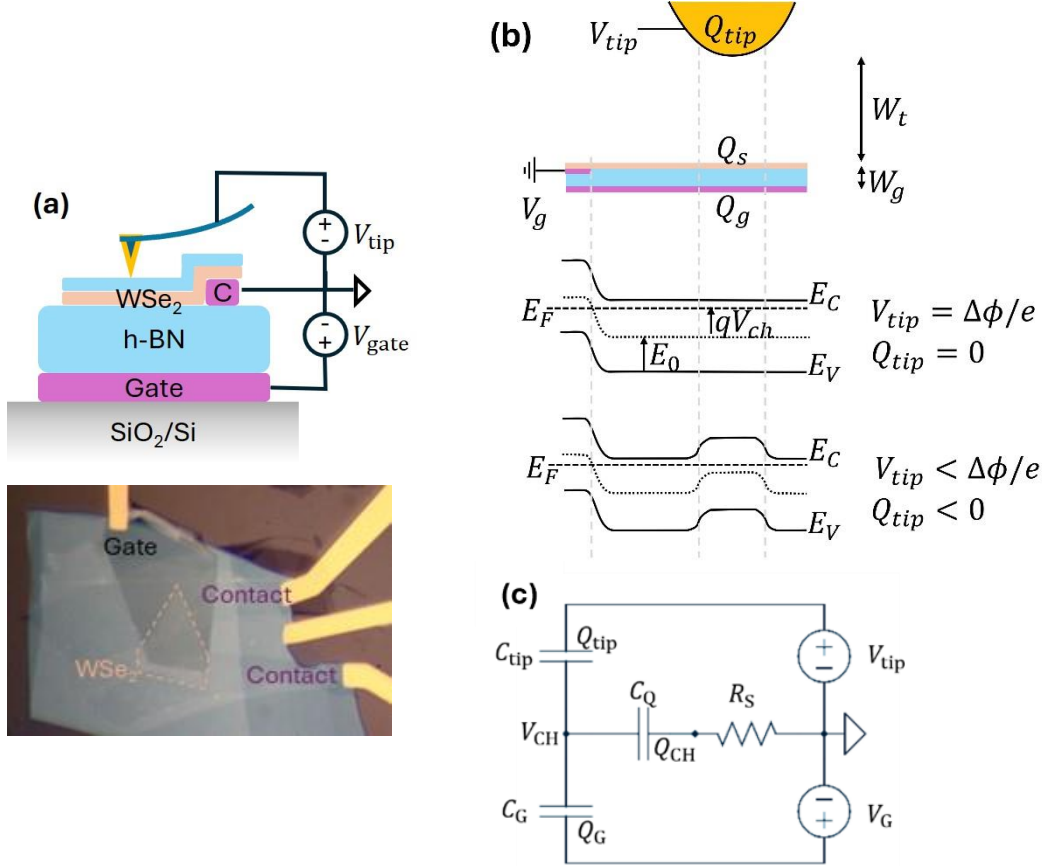


Figure 1. Experimental setup. **(a)** Above: schematic showing the typical sample stack with electrical connections to tip and gate voltages, V_{tip} and V_g , where 'C' represents the grounded source/drain contacts to the WSe₂. Below: optical image of sample A. The monolayer WSe₂ channel is outlined for better visibility. **(b)** Schematic cross-section of the tip near the sample. The upper band diagram corresponds to the 2DSC with $V_g > 0$, putting E_F near the conduction band. When the tip is biased to be neutral, it produces no band bending. The lower band diagram shows band bending near the tip when V_{tip} is more negative. In this geometry, at the contact, the gate dopes the underlying graphite flake, which carries current to the gold pads. **(c)** Schematic circuit diagram relating charges on the tip, gate, and channel (Q_{tip} , Q_g , and Q_{CH} respectively) to V_{tip} and V_g voltages and the channel potential V_{CH} . The quantum capacitance C_Q embodies the nonlinear charge-potential relation of the channel (see text).

zero-charge condition occurs at $V_{tip} = V_0 = \Delta E_F + V_S$, where ΔE_F equals the tip-sample work function difference $\Delta\phi$ and V_S is the bias applied to the sample (typically, but not necessarily, zero). This condition assumes there is negligible potential offset due to fixed space charges in any dielectric present between the tip and the sample.

In the simple AM-KPFM technique, the tip motion at ω_e is minimized. Other technique variants minimize the tip motion at sum or difference frequencies (sideband, heterodyne),

or detect the resonance frequency modulation resulting from the tip motion (FM-KPFM) [16]. In these variants, the detected signal remains proportional to $V_{DC} - V_0$, so our general discussion continues to be relevant, but the signal falls off more rapidly with distance, minimizing contributions from stray fields and allowing V_0 to be determined more accurately [17,18]. With these techniques, KPFM can be used to map spatial variations in E_F , such as those induced by gate doping of graphene [19].

Our experiments were conducted with an Oxford Cypher probe microscope using dual-pass FM-KPFM. For each scan line, a first sweep measures the topography with the average tip height typically at $W_T = 50$ nm. In a second sweep, the tip follows the established topography at the same W_T but with the mechanical oscillation amplitude reduced to $\sim 20\%$ of the initial value (~ 10 nm) so the tip-sample interaction is attractive, and the KPFM signal is measured.

Figure 1a shows a cross-sectional schematic and an image of a typical device consisting of WSe₂ back-gated through hBN of thickness W_g . The multi-layer graphene gate electrode and the few-layer graphene contacts each connect to gold pads. The flakes were mechanically exfoliated, mainly using commercial crystals from 2D Semiconductors [20], and stacked using standard dry-polymer transfer techniques [21]. Thicknesses were measured with tapping mode atomic force microscopy. Of four monolayer WSe₂ devices (A-D), all having $W_g \sim 20$ nm, samples A,B,C were encapsulated with few-layer hBN on top of the WSe₂ while D was not. A fifth device (E) consists of unencapsulated 3-layer WSe₂ with $W_g = 115$ nm.

Measurements were conducted under ambient conditions with the contacts to the channel electrically grounded. The KPFM signal was analyzed by averaging data from each distinct region, avoiding large bubbles or other obvious defects. Averaged data typically had standard deviations ~ 50 mV. Example KPFM images, taken with $\tilde{V}_{tip} = 3$ V, are shown in Fig. 2, along with summative data.

In the exposed hBN region, we expect V_{KP} to simply track the potential of the underlying graphite flake and thus the gate bias V_g . All measured values of dV_{KP}/dV_g were indeed in the range 0.95 to 1.05. The $V_g = 0$ intercept, interpreted as ΔE_F , averaged +0.13 V for the Ti/Ir-coated tip (AsyElec 01.R2) we used for most measurements, and was consistent with the $V_g = 0$ measurement on the contact. Measurements of V_{KP} from the rest of the sample were then normalized by subtracting the $V_g = 0$ intercept to make them, in principle, relative to the work function of multilayer graphene.

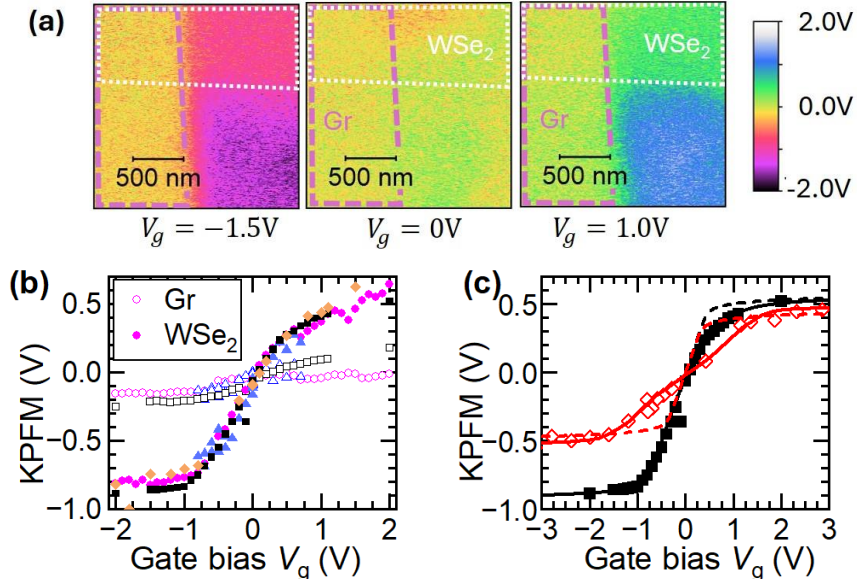


Figure 2. (a) KPFM maps of sample C for varying gate bias, showing the WSe₂ channel and its bilayer graphene contact, as well as, at the lower right of each image, the exposed hBN with the gate electrode underneath. (b) Trends in KPFM signal with gate bias for monolayer WSe₂ samples: A \diamond , B \circ , C \blacksquare , and D \blacktriangle . Open symbols represent the contact region (labelled Gr), and closed symbols are WSe₂. (c) Data showing the impact of thin (sample C \blacksquare) versus thick (E \diamond) gate dielectrics on KPFM response. Sample E has 3-layer WSe₂, and its reduced bandgap is apparent. A simple model (dashed lines) is improved for sample C by including exponential band tail states (black line), or for sample E by including the nonlinear KPFM response of the 2DSC (red line).

The goal is to relate V_{KP} to the local value of E_{F} in the 2DSC under the tip. A full three-dimensional self-consistent model would include factors such as tip shape and spatially resolved tip-sample interactions, as well as a complete 3D band model [22]. For a simple but practical approximation, we consider only a planar geometry, neglecting lateral variation in the sample and tip curvature, and take the charge response of the sample to be instantaneous, i.e., we assume electrostatic equilibrium under the tip. Our results below justify these assumptions.

In this model, the charges on the tip, Q_{tip} , and gate, Q_g , determine the charge on the sample, $Q_{\text{tip}} + Q_g = -Q_S$, which is linked to E_{F} in the 2DSC. In accord with standard practice, we define the channel potential V_{CH} as the value of E_{F} relative to the midgap energy; thus $E_{\text{C}} - E_{\text{F}} = E_0 - qV_{\text{CH}}$ and $E_{\text{F}} - E_{\text{V}} = E_0 + qV_{\text{CH}}$, where E_{C} and E_{V} are the conduction and valence band energies, respectively, $E_0 = (E_{\text{C}} - E_{\text{V}})/2$, and q is the elementary charge, as shown in Fig. 1b. In Fig. 1c we also give a schematic illustration of the relationship between these quantities that can be useful in visualizing the charge-voltage relationship. Tip and gate capacitances (per area), C_{tip} and C_g respectively, were estimated with a planar model using measured W_g , W_{tip} , and hBN cap thickness, and an

hBN dielectric constant of 3.9. The schematic also includes the quantum capacitance $C_Q = -\partial Q_S / \partial V_{\text{CH}}$ to conceptually illustrate the relationship between Q_S and V_{CH} . It should be noted, however, that C_Q is an imaginary, nonlinear capacitance. We must calculate the relationship between Q_S and V_{CH} directly within the model.

The electron and hole densities are given by

$$n = \int_{E_C}^{\infty} g_{2\text{D}}^e f(E) dE = g_{2\text{D}}^e kT \ln\{1 + \exp[-(E_0 - qV_{\text{CH}})/kT]\} \quad (4a)$$

$$p = \int_{-\infty}^{E_V} g_{2\text{D}}^h f(E) dE = g_{2\text{D}}^h kT \ln\{1 + \exp[-(E_0 + qV_{\text{CH}})/kT]\} \quad (4b)$$

with Boltzmann constant k , temperature T and Fermi-Dirac distribution $f(E)$. Here, $g_{2\text{D}}^e$ ($g_{2\text{D}}^h$) is the constant 2D electron (hole) density of states, given by $\pi g_s g_v m_e^*/\hbar^2$, where g_s and g_v are the spin and valley degeneracies and m_e^* (m_h^*) is the electron (hole) effective mass; we used $g_s = g_v = 2$ and $m_e^* = m_h^* = 0.4m_e$. Using values of the bandgaps of 1.65 eV for monolayer WSe₂ and 1.2 eV for 3-layer WSe₂ from the literature [23,24,25] gave very good fits (see below). The value of V_{CH} at $V_g = 0$, V_{CHi} , represents possible offsets by nonideal effects like stray charge in the oxide. We used Eq. 4 to relate p_i and n_i , the carrier densities at $V_g = 0$, to V_{CHi} .

Balancing the charges then gives

$$C_T [V_{\text{tip}} - (V_{\text{CH}} - V_{\text{CHi}})] + C_g [V_g - (V_{\text{CH}} - V_{\text{CHi}})] = q[(p - p_i) - (n - n_i)]. \quad (5)$$

To begin with, we took $Q_{\text{tip}} = 0$, representing an ideal KPFM measurement, and solved Eq. 5 numerically for V_{CH} as a function of V_g (dashed lines in Fig. 2d). The V_{CHi} was treated as an adjustable fitting parameter; it offsets the curve but does not change its shape, and was less than 0.2 eV for all samples.

For devices with $W_g = 20\text{nm}$, this very simple model fit the data surprisingly well. We found that the data for all monolayer devices could be fit better by adding an exponentially distributed “defect band” of electron acceptors near the conduction band edge:

$$n_{\text{trap}} = a g_{0\text{T}} \exp[-(E_0 - qV_{\text{CH}})/a]. \quad (6)$$

The calculations shown in Fig. 2d (black solid line) use $g_{0\text{T}} = 1.4 \times 10^{13} \text{ cm}^{-2} \text{ eV}^{-1}$ and $a = 0.2 \pm 0.02 \text{ eV}$, values consistent with prior measurements on MoS₂, where the defects were postulated to be S vacancies [8]. The defect band slows the tuning of E_F into the upper half of the bandgap and immobilizes much of the negative charge, degrading the transistor characteristics.

Although this simple model yields an excellent fit for devices with $W_g = 20$ nm, it is insufficient for devices with thicker gate dielectrics. This is evident from the data on device E. To investigate the effect of nonlinear response of the 2DSC on the KPFM measurement, the full expression of Eq. 5 was used with the first term nonzero. The value of V_{CH} was resolved at 100 points through the AC cycle, and averaged to yield the DC Fourier component $\langle V_{\text{CH}} \rangle$; this process was repeated while iterating V_{DC} until $\langle V_{\text{CH}} \rangle = V_{\text{DC}}$. The final value is the modeled output V_{KP} . As expected, the bands can be bent significantly by \tilde{V}_{tip} , and the resulting asymmetry introduces an additional DC component that must be allowed for, as can be seen in Fig. 3.

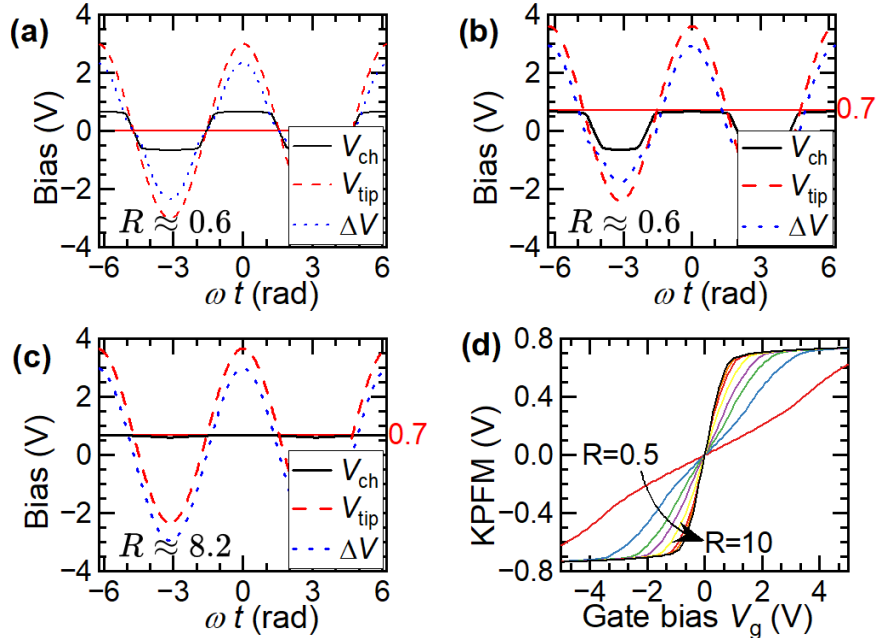


Figure 3. Simulations of the time-varying tip and channel voltage (V_{tip} , V_{ch}) under varying conditions for gated, undoped, monolayer WSe₂. The tip's mechanical response is driven by $\Delta V = V_{\text{tip}} - V_{\text{ch}} = Q_{\text{tip}}/C_{\text{tip}}$. In (a-c), the DC component of V_{tip} equals V_0 , the ideal KPFM signal. **(a)** Simulation of WSe₂ with 285 nm gate dielectric, $V_g = 0$ V, and $V_0 = 0$ V. Although V_{CH} is driven near the band edges by the tip bias, it averages to 0 V and will not affect the KPFM result. **(b)** Like (a), but with $V_g = 1$ V, resulting in $V_0 = 0.67$ V. This causes V_{CH} to oscillate asymmetrically around 0; its time-averaged value is 0.42 V, which would cause an incorrect KPFM reading. **(c)** WSe₂ gated through a 20 nm dielectric, with $V_g = 1$ V, and $V_0 = 0.67$ V. The larger ratio of gate to tip capacitance, R , divides the V_{CH} response, minimizing the effect of asymmetry. **(d)** Simulated KPFM response for devices with $R = 0.5, 1, 1.5, 2, 3, 5, 7$, and 10. For $R \gtrsim 3$, the KPFM signal would accurately reflect V_0 , within typical measurement uncertainty. These simulations use a bandgap of 1.65 V, and V_{CH} continues increasing very slowly for larger V_g .

This calculation fits the sample E data well (solid red line, Fig 2d), with no adjustable parameters except for $V_{\text{CHi}} = 0.05$ eV. So, even though V_{KP} does not quantitatively yield V_{CH} in this case, useful information can still be extracted. There is no straightforward way to predict the resulting KPFM signal, because changing V_{DC} also affects the charge on the gate, Q_g . However, the presence of nonlinear effects can be quickly identified from a mid-gap slope, dV_{KP}/dV_g , smaller than one.

To further understand this response, consider only the time-varying part of the channel voltage, \tilde{V}_{CH} , where

$$\tilde{V}_{\text{CH}} = \left(1 + \frac{C_Q + C_g}{C_{\text{tip}}}\right)^{-1} \tilde{V}_{\text{tip}}. \quad (7)$$

This expression does not give a simple proportionality between \tilde{V}_{CH} and \tilde{V}_{tip} because C_Q changes during the AC cycle. However, if $R = C_g/C_{\text{tip}} \gg 1$ then \tilde{V}_{CH} is divided down accordingly, minimizing any asymmetrical response due to C_Q .

Fig. 3 compares the modeled channel response for varying R . Using a planar capacitor model, samples A-D have $R = 8.2$, making the error induced by asymmetry 3 mV, much less than the uncertainty in the measurement itself. This explains why KPFM yields quantitatively correct results for samples A-D, and not for sample E ($R = 2.0$).

Our work shows that KPFM measurements of 2DSCs can, in fact, provide quantitatively correct measurements on semiconductor device structure. For the best results, one should use a thin gate dielectric and a sufficient tip lift height that the gate-channel capacitance is much larger than the tip-channel capacitance. Then, with a sweep of gate voltage one can assess parameters including the effectiveness of gating, sample bandgap, potential barriers at contacts, band-edge defects densities, and spatial nonuniformity. Moreover, even when the gate dielectric is thick, the KPFM signal will still be accurate in regimes where C_Q is large, i.e., at high doping levels, and the nonlinear response at lower doping levels can also be modeled with our simple iterative approach.

The authors have no conflicts to disclose.

The data that support the findings of this study are available from the corresponding author upon reasonable request.

Acknowledgements

Thanks to Jay Ewing for assistance with design, machining, and fabrication, and to Keith Jones for guidance on the Cypher instrument and KPFM. J.H., J.M., and J.T.-U. were supported by the Murdock Charitable Trust Awards 202118943 and 2017319, as well as by the National Science Foundation (NSF) under DMR-MRI-1827971. N.R. was funded by the NSF DMR-2226592. Work at the University of Washington was supported by National Science Foundation (NSF) MRSEC award 2308979, and by Programmable Quantum Materials, an Energy Frontier Research Center funded by the U.S. Department of Energy (DOE), Office of Science, Basic Energy Sciences (BES), under award DE-SC0019443. The authors thank Dr. Ronen Dagan and Yossi Rosenwaks for sharing data and information.

References

- [1] Chen, J., Wang, W., Yan, X., “Two-dimensional material-based devices for in-sensor computing,” *npj Unconv. Comput.* **2**, 19, 2025. <https://doi.org/10.1038/s44335-025-00034-4>
- [2] Yoon, H.H., Park, J.Y., Megra, Y.T., Baek, J.H., Song, M., Akinwande, D., Ha, D., Kang, D.-H., Shin, H.-J., “Enabling the Angstrom Era: 2D material-based multi-bridge-channel complementary field effect transistors,” *npj 2D Mater Appl* **9**, 68, 2025. <https://doi.org/10.1038/s41699-025-00591-z>
- [3] Nakatsuji, N., Kawakami, T., Tateishi, H., Kato, K., Koshino, M., “Moiré band engineering in twisted trilayer WSe₂,” *Commun Mater* **6**, 274, 2025. <https://doi.org/10.1038/s43246-025-00996-9>

[4] W. Melitz, J. Shen, A. C. Kummel, S. Lee, “Kelvin probe force microscopy and its application,” *Surface Science Reports* **66**, 1-27, 2011.

<https://doi.org/10.1016/j.surfrep.2010.10.001>

[5] V. Panchal, R. Pearce, R. Yakimova, A. Tzalenchuk, O. Kazakova, “Standardization of surface potential measurements of graphene domains,” *Scientific Reports* **3**, 2597, 2013.

<https://doi.org/10.1038/srep02597>

[6] Y.-J. Yu, Y. Zhao, S. Rya, L.E. Brus, K.S. Kim, P. Kim, “Tuning the graphene work function by electric field effect,” *NanoLetters* **9**, 3430-3434, 2009.

<https://doi.org/10.1021/nl901572a>

[7] J. Yu, R. Giridharagopal, Y. Li, K. Xie, J. Li, T. Cao, X. Xu, and D.S. Ginger *NanoLetters* **21**, 3280-3286, 2021. DOI: 10.1021/acs.nanolett.1c00609

[8] J. Xu and D. Chen, “Interpreting Kelvin probe force microscopy on semiconductors by Fourier analysis,” *J. Appl. Phys.* **129**, 034301 (2021) <https://doi.org/10.1063/5.0024073>

[9] X. Sun, Y. Chen, Z. Li, Y. Han, Q. Zhou, B. Wang, T. Taniguchi, K. Watanabe, A. Zhao, J. Wang, Y. Liu, J. Xue, “Visualizing Band Profiles of Gate-Tunable Junctions in MoS₂/WSe₂ Heterostructure Transistors,” *ACS Nano* **15**, 16314–16321, 2021.

<https://doi.org/10.1021/acsnano.1c05491>

[10] M. Raturi, A. Kundu, R. Rani, J. Saini, K.S. Hazra, “Tracking electronic band alignment across 2D bridge-channel MoS₂ during charge transport,” *Appl. Phys. Lett.* **121**, 013101 2022. <https://doi.org/10.1063/5.0082408>

[11] D. Dumcenco, D. Ovchinnikov, K. Marinov, P. Lazić, M. Gibertini, N. Marzari, O. Lopez Sanchez, Y.-C. Kung, D. Krasnozhon, M.-W. Chen, S. Bertolazzi, P. Gillet, A. Fontcuberta i Morral, A. Radenovic, A. Kis, “Large-area epitaxial monolayer MoS₂” ACS Nano **9**, 4611-4620, 2015. <https://doi.org/10.1021/acsnano.5b01281>

[12] K. Chen, X. Wan, J. Wen, W. Xie, Z. Kang, X. Zeng, H. Chen, J.-B. Xu, “Electronic properties of MoS₂-WS₂ Heterostructures synthesized with two-step lateral epitaxial strategy,” ACS Nano **10**, 9868-9876, 2015. <https://doi.org/10.1021/acsnano.5b03188>

[13] M. Kim, J. Park, D. Lee, J. Kim, “Phosphorus-ion implantation in two-dimensional WSe₂ for hole doping,” J. Vac. Sci. Technol. A 43, 050402 (2025)

<https://doi.org/10.1116/6.0004797A>

[14] R. Dagan, Y. Vaknin, Y. Rosenwaks, “Gap state distribution and Fermi level pinning in monolayer to multilayer MoS₂ field effect transistors,” Nanoscale **12**, 8883–8889, 2020. <https://doi.org/10.1039/D0NR01379J>

[15] D. Jeon, H. Kim, M. Gu, T. Kim, “Imaging Fermi-level hysteresis in nanoscale bubbles of few-layer MoS₂,” communications materials **4**, 62, 2023. <https://doi.org/10.1038/s43246-023-00388-x>

[16] Y.J. Li, H. Wen, Z.M. Ma, L. Kou, Y. Naitoh, Y. Sugawara, “Kelvin Probe Force Microscopy with Atomic Resolution,” in: S. Sadewasser, T. Glatzel (Eds.), *Kelvin Probe Force Microscopy: From Single Charge Detection to Device Characterization*, Springer Series in Surface Sciences. Springer International Publishing, Cham, pp. 437–463, 2018.

https://doi.org/10.1007/978-3-319-75687-5_14

[17] J. Xu, G. Bai, J. Li, W. Li, “Inhomogeneous probe surface induced effect in Kelvin probe force microscopy,” *J. Appl. Phys.* **127**, 184302, 2020. <https://doi.org/10.1063/5.0005276>

[18] Z.M. Ma, L. Kou, Y. Naitoh, Y.J. Li, Y. Sugawara, “The Stray Capacitance Effect in Kelvin Probe Force Microscopy Using FM, AM and Heterodyne AM Modes,” *Nanotechnology* **24**, 225701, 2013. <https://doi.org/10.1088/0957-4484/24/22/225701>

[19] Y.-J. Yu, Y. Zhao, S. Ryu, L.E. Brus, K.S. Kim, P. Kim, “Tuning the Graphene Work Function by Electric Field Effect,” *Nano Lett.* **9**, 3430–3434, 2009. <https://doi.org/10.1021/nl901572a>

[20] 2D Semiconductors, <https://2dsemiconductors.com/>

[21] P.J. Zomer, M.H.D. Guimarães, J.C. Brant, N. Tombros, B.J. van Wees, “Fast pick up technique for high quality heterostructures of bilayer graphene and hexagonal boron nitride,” *Appl. Phys. Lett.* **105**, 013101, 2014. <https://doi.org/10.1063/1.4886096>

[22] R.K.A. Bennett, E. Pop, “How Do Quantum Effects Influence the Capacitance and Carrier Density of Monolayer MoS₂ Transistors?” *Nano Lett.* **23**, 1666–1672, 2023. <https://doi.org/10.1021/acs.nanolett.2c03913>

[23] H. Zhou, C. Wang, J.C., Shaw, R. Cheng, Y. Chen, X. Huang, Y. Liu, N.O. Weiss, Z. Lin, T. Huang, X. Duan, “Large Area Growth and Electrical Properties of p-Type WSe₂ Atomic Layers. *Nano Lett.* **15**, 709–713, 2015. <https://doi.org/10.1021/nl504256y>

[24] Nguyen, P.V., Teutsch, N.C., Wilson, N.P., Kahn, J., Xia, X., Graham, A.J., Kandyba, V., Giampietri, A., Barinov, A., Constantinescu, G.C., Yeung, N., Hine, N.D.M., Xu, X., Cobden,

D.H., Wilson, N.R., “Visualizing electrostatic gating effects in two-dimensional heterostructures,” *Nature* **572**, 220–223, 2019. <https://doi.org/10.1038/s41586-019-1402-1>

[25] Sun, Y., Wang, D., Shuai, Z., “Indirect-to-Direct Band Gap Crossover in Few-Layer Transition Metal Dichalcogenides: A Theoretical Prediction,” *J. Phys. Chem. C* **120**, 21866–21870, 2016. <https://doi.org/10.1021/acs.jpcc.6b08748>